LUND UNIVERSITY

Investigation of photochemical effects in flame diagnostics with picosecond photofragmentation laser-induced fluorescence

Jonsson, Malin; Larsson, Kajsa; Borggren, Jesper; Aldén, Marcus; Bood, Joakim

Investigation of photochemical effects in flame diagnostics with picosecond photofragmentation laser-induced fluorescence

Malin Jonsson*, Kajsa Larsson, Jesper Borggren, Marcus Aldén, Joakim Bood

Division of Combustion Physics, Department of Physics

Lund University, Box 118, 221 00 Lund, Sweden

*Corresponding author: Malin Jonsson

Email: malin.jonsson@forbrf.lth.se

Phone: +46 46 222 31 08

Keywords: Photofragmentation, Laser-induced fluorescence, Combustion diagnostics, Comparison picosecond and nanosecond excitation, Hydroperoxyl radical

Abstract

Photofragmentation laser-induced fluorescence (PFLIF) is for the first time performed based on picosecond laser pulses for detection of hydroperoxyl radicals (HO_2) in a stoichiometric laminar methane/air flame. Photofragmentation is performed with a pump laser pulse of 80 ps duration and a wavelength of 266 nm, whereupon the produced OH photofragments are detected by a second picosecond probe laser pulse, inducing fluorescence via excitation in the $A^2\Sigma^+(v=1) \leftarrow X^2\Pi(v=0)$ band of OH near 283 nm. Excitation spectra of the OH photofragments formed in the reaction zone were recorded for pump-probe delays ranging from 0 to 5 ns. The spectra suggest that the population distribution of the nascent OH fragments is rotationally cold and that it takes on the order of 5 ns for the nascent non-equilibrium rotational distribution to relax into a thermal distribution. The radial OH-fragment distribution was extracted from spectral images (radial position vs emission wavelength) recorded at six different pump-probe delays. Photochemical OH production was observed both in the reaction zone and the product zone. Comparison with a kinetic model for OH production suggests that more than 20% of the oxygen fragments produced by photolysis in the reaction zone are formed in the excited ^1D state, explaining a very rapid initial signal growth. The OH-production model was also compared with previous reaction-zone data, acquired with nanosecond laser pulses in the same flame, indicating that no $O(^1D)$, but only $O(^3P)$, is formed. A plausible explanation of the discrepancy between the two results is that the picosecond pulses, having more than two-orders of magnitude higher irradiance than the nanosecond pulses used in the previous study, might cause 2-photon photodissociation, allowing production of $O(^1D)$. In terms of flame diagnostics with PFLIF, it is concluded that a setup based on nanosecond laser pulses, rather than picosecond pulses, appears preferable since photochemical OH production in the reaction zone can be avoided while for short delay times the ratio between the photofragment signal and the photochemical interference in the

product zone, stemming from CO_2 photolysis, is sufficiently large to clearly visualize the photofragments.

1. Introduction

Hydrogen peroxides (HO_2 and H_2O_2) are important intermediate species in various oxidation processes, e.g. in plasma, combustion, and atmospheric chemistry. In the troposphere, OH is the most important oxidant and it is primarily produced from photolysis of O_3, and its chemistry is closely linked to HO_2 and H_2O_2 [1, 2]. In hydrocarbon combustion, H_2O_2 and HO_2 are important flame intermediates playing a key role in the low-temperature (<1200 K) oxidation of the fuel [3]. In H_2/O_2 combustion, the reaction $H_2 + O_2 \rightarrow HO_2 + H$ initiates chain branching and is thus of great significance [4]. Furthermore, the thermal decomposition of hydrogen peroxide is a pivotal chain-branching reaction in combustion engine concepts based on autoignition [5-7], for example the homogenous charge compression ignition (HCCI) engine, which relies on simultaneous autoignition at multiple locations [8]. It is evident that there is a strong need for techniques able to detect H_2O_2 and HO_2 in-situ with high species selectivity as well as high spatial and temporal resolution.

Hydrogen peroxides have been detected with various absorption-spectroscopic techniques [9-16]. Recently, Sajid et al. used mid-infrared absorption spectroscopy near 7.7 μm to measure the rate of hydrogen peroxide decomposition behind reflected shock waves [17]. Absorption-based techniques are attractive for measuring absolute species concentrations since the signal is unaffected by predissociation and quenching. The measured absorption signal is, however, integrated along a line of sight and measurements are therefore restricted to volumes in which variations in concentrations and temperatures along the line of sight are insignificant.

Laser-induced fluorescence (LIF) is a popular technique for combustion diagnostics since it offers the possibility to measure concentrations of trace species with high temporal and spatial resolution [18, 19]. In particular its ability to deliver two-dimensional snapshot visualizations makes LIF very attractive for combustion studies, where the conditions often

are turbulent. Unfortunately, the electronic structure of HO_2 and H_2O_2 prevents direct detection with LIF based on electronic excitation [20] due to the unbound excited electronic states, and UV excitation hence leads to dissociation into fragments [21]. It is, however, possible to indirectly visualize hydrogen peroxides using LIF as a probe for OH photofragments created by a preceding dissociative UV laser pulse. This pump-probe technique is called photofragmentation laser-induced fluorescence (PFLIF) [22-24].

Previously, our group has developed and demonstrated PFLIF based on nanosecond (ns) laser pulses for two-dimensional imaging of H_2O_2 in an HCCI engine [25, 26] and HO_2 in laminar flames [27]. Recently we have shown the possibility to combine structured illumination with PFLIF to visualize hydrogen peroxides on a single-shot basis [28]. In the flame study, a photochemically induced OH signal, originating from photolysis of hot CO_2, was observed in the product zone of the flame [27]. It was concluded that hot CO_2 is photodissociated by the pump pulse into CO and O, whereupon the oxygen atoms form OH upon reactions with H_2O or H_2. The intensity of this unwanted interfering signal was found to increase with increasing pump-probe delay up to a delay of ~1 µs, where the signal starts to decrease with increasing delay (see Fig. 10a in [27]). It was also observed that the intensity of the signal-of-interest, i.e. OH fluorescence stemming from photolysis of HO_2 present in the reaction zone, increases by ~25% as the pump-probe delay increases from 10 to 200 ns (see Fig. 10b in [27]). The reason for this intensity growth was not discussed in [27]. Nevertheless, in addition to OH fragments, photodissociation of HO_2 produces an equal amount of oxygen atoms, i.e. $HO_2 + h\nu \rightarrow OH + O$, in the reaction zone of the flame. Hence, it is possible that OH fragments are produced photochemically as these oxygen atoms react with hydrogen-containing species, such as methane (CH_4) and H_2O.

The oxygen atom can be formed either in its [3]P ground state or in the excited [1]D state. For 220-nm photolysis at room temperature Sinha et al. found that ~87% of the oxygen atoms are

5

formed in the ^{1}D state [29]. Lee et al. have also investigated O(^{1}D) production upon photodissociation of HO$_2$ at 193 and 248 nm [30, 31]. They monitored the fluorescence emitted from O$_2$(b$^1\Sigma_g^+$), which is produced by the collisional energy transfer process O(^{1}D) + O$_2$(X$^3\Sigma_g^+$) $\rightarrow$ O(^{3}P) + O$_2$(b$^1\Sigma_g^+$), to estimate the production of O(^{1}D). Lee et al. concluded that UV photolysis of HO$_2$ primarily produces oxygen atoms in the ^{1}D state [31]. In order to understand the origin of the increasing signal in the reaction zone, as well as investigating the early buildup of the product zone interference, pump-probe studies with delays significantly shorter than allowed by nanosecond pulses are needed.

In the present work, PFLIF experiments based on picosecond (ps) laser pulses, allowing sub-nanosecond pump-probe delay times, have been performed in a laminar stoichiometric methane/air flame at atmospheric pressure. The pump pulse is of 266-nm wavelength, while the wavelength of the probe pulse is tunable, allowing OH fragment excitation spectra to be recorded at different pump-probe delays. These excitation spectra reveal the rotational population dynamics of the produced OH (X$^2\Pi$) photofragments, which to the best of our knowledge, has not been studied in atmospheric flames previously. Furthermore, spectrally dispersed fluorescence along a horizontal line through the flame was recorded for a set of pump-probe delays. These data provide information about the temporal development of the OH fragment signal in the reaction and product zone, respectively. An analytical expression for OH production in the reaction zone, based on both O(^{3}P) and O(^{1}D) reactions, was derived. Experimental data recorded in this work, using picosecond laser pulses, as well as previously recorded data, based on nanosecond laser pulses, are compared with simulated OH fragment production curves based on the aforementioned expression. From these comparisons it is possible to estimate O(^{3}P)/O(^{1}D) branching ratios for the two cases.

The paper is structured as follows: following this introduction, the experimental arrangement is described followed by a description of the model for photochemical OH

production in the reaction zone. Then the results are presented and discussed, before the paper ends with a section summarizing the major conclusions of the study.

2. Experimental setup

The experimental setup for picosecond PFLIF is schematically displayed in Fig. 1. The fundamental output from a mode-locked Nd:YAG laser (Ekspla, PL-2143C), providing pulses of 80-ps duration at a 10-Hz pulse repetition rate, is frequency quadrupled to 266 nm, providing the photolysis/pump pulses. The residual fundamental radiation is amplified (Ekspla, APL70-1100) and converted into 355 nm by frequency tripling to pump an optical parametric generator/amplifier system (OPG/OPA, Ekspla PG 401-P80-SH). The OPG/OPA system provides tunable probe pulses across the OH $A^2\Sigma^+(v=1) \leftarrow X^2\Pi(v=0)$ band (~282–285 nm) with a linewidth of ~5 cm^{-1} and with a minimum wavelength increment of 0.05 nm. The spectral resolution of the excitation spectra was determined by the convolution of these limiting factors and was found to be ~8.3 cm^{-1}. The pulse energy of the pump laser was roughly 5 mJ, except during the excitation scans when it was slightly lower (3.5 mJ). The pulse energy of the probe laser was varying between 0.3-0.7 mJ depending on the wavelength.

The pump and probe pulses were spatially overlapped by a dichroic mirror (DM) and focused over the center of the burner by a spherical lens. In this work mainly two studies were performed; first excitation spectra recorded at different pump-probe delays were investigated and, second, the induced photofragment signal was studied at different pump-probe delays with the probe laser set at a fixed wavelength. A spherical lens with a focal length of 500 mm was used for the excitation scans, while a focal length of 300 mm was used in the pump-probe delay studies. The 300- and 500-mm lenses gave a 266-nm laser diameter of 140 and 400 µm, respectively in the focus, while both lenses resulted in a diameter of 500 µm for the probe beam. The reason why a lens with a shorter focal length was used in the latter case is because

a smaller focal spot enhances the photochemical interference in the product zone, which is important in order to demonstrate how this contribution depends on the pump-probe delay as clearly as possible. The time delay between the pump and probe pulse was variable between 0-5 ns via an adjustable optical delay line, calibrated by streak camera measurements. By guiding the pump pulse outside the optical delay line, delays of 12.5 ns and 22.5 ns could be realized as well. The OH-LIF signal ($A^2\Sigma^+$(v=0) $\rightarrow$ $X^2\Pi$(v=0)) was collected at right angle relative to the direction of the laser beams and spectrally filtered with a band-pass filter (λ_{center}=307 nm, FWHM=10 nm) in combination with a liquid N,N-dimetylformamide filter. For the excitation spectra, the signal was imaged with an intensified CCD camera (Princeton Instruments, PI-MAX III) equipped with a UV-objective (B-Halle, f = 100, f/2). The camera gate was 30 ns and the timing was synchronized with the arrival of the pump pulse.

The spectrally resolved emission measurements were carried out using a 0.5-m focal length spectrograph (Princeton Instruments, Acton Model SP-2556). The spectrograph had a 1200 grooves/mm grating, blazed at 300 nm, and a horizontal slit with a width set to 100 µm, and an intensified CCD camera (Princeton Instruments, PI-MAX III 1024x1024 pixels). Neglecting any diffraction effects and aberrations, an instrument line profile of a trapezoid with 0.04 nm full width at half maximum (FWHM) was estimated. The pixels were binned in the vertical direction giving images with a size of 1024x512 pixels. In these measurements, the camera gate was 50 ns and the timing was synchronized with the arrival of the pump pulse.

The measurements were conducted at atmospheric pressure in a stoichiometric premixed laminar CH_4/air flame 1.5 cm above a burner consisting of two coaxial tubes with 2.2 and 22 mm diameter, respectively. The gas speeds in the inner and outer tubes were 12 and 0.4 m/s, respectively, and the gas composition was controlled by calibrated mass flow controllers (Bronkhorst). To reduce the influence of laser power variations and flame fluctuations during

the measurements, every second pump pulse was blocked by a chopper running at 5 Hz. Thus every other image contains signal from both the naturally present OH and OH fragments as well as prompt signal induced by the pump laser (PFLIF image), while the other images holds signal from only naturally present OH (LIF image). A second data set was acquired with the probe laser blocked. Here, every other image contains prompt signal induced by the pump pulse and background signal (Pump image), while the other images only contain background signal (Background image). The image of interest (IOI), i.e. the image containing only fluorescence from OH fragments, was extracted through the following operation:

IOI = PFLIF image – LIF image – (Pump image – Background image),

and typically 2000 images were recorded in each data set. Before each measurement, the spatial overlap of the pump and probe beams was carefully optimized by maximizing the PFLIF signal generated in a free flow of a vaporized H_2O_2 generated by bubbling nitrogen gas through a liquid mixture of 50:50 wt.% H_2O_2:H_2O. The probe laser intensity was low enough to obtain OH fluorescence that was linearly dependent on the laser intensity.

The energies of the probe pulses were monitored by a photo-diode, allowing compensation for fluctuations in the probe laser energy. Such compensation was carried out on the recorded excitation spectra, since the pulse energy of the probe laser varies when the wavelength is changed.
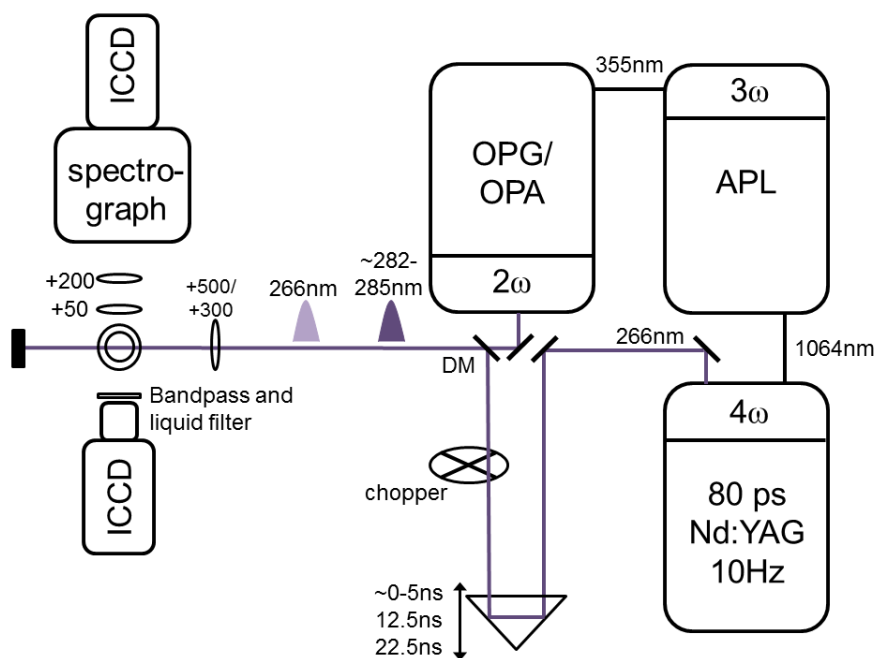
Fig. 1 Schematic illustration of the experimental setup. The pump (266 nm) and probe (282-285 nm) pulses were overlapped via a dichroic mirror (DM) and focused above the burner by a spherical lens of 500-mm or 300-mm focal length. The fluorescence signal was either analyzed spectrally dispersed using a spectrograph or imaged directly with an ICCD camera.

3. Model for photochemical OH production in the reaction zone

Photodissociation of HO_2, i.e. $HO_2 + h\nu \rightarrow OH + O$, produces equal amounts of OH and oxygen atoms. Assuming that the only significant contribution of OH production from the oxygen atom comes from interaction with H_2O and CH_4 the following reactions are expected:

$$O(^3P,{}^1D) + H_2O \xrightarrow{k_1^P, k_1^D} OH + OH \tag{1}$$

$$O(^3P,{}^1D) + CH_4 \xrightarrow{k_2^P, k_2^D} CH_3 + OH \tag{2}$$

The superscripts P and D designate rate constants corresponding to $O(^3P)$ and $O(^1D)$, respectively. For $O(^1D)$, deactivation to $O(^3P)$ through collisions with nitrogen and oxygen molecules have to be accounted for as well:

$$O(^1D) + N_2 \xrightarrow{k_3} O(^3P) + N_2 \tag{3}$$

10

$$O(^1D) + O_2 \xrightarrow{k_4} O(^3P) + O_2 \tag{4}$$
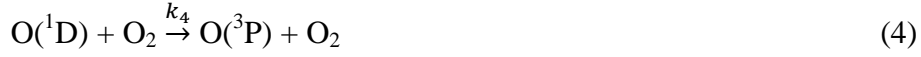
For a stoichiometric laminar premixed CH_4/air flame, chemical kinetics modeling using the Konnov detailed C/H/N/O mechanism [32] predicts a HO_2 concentration peak of 8.2×10^{14} molecules/cm^3, and at this location, the model also predicts the following major species concentrations: $[H_2O] = 4.1 \cdot 10^{17}$ molecules·cm^{-3}, $[CH_4] = 7.5 \cdot 10^{17}$ molecules·cm^{-3}, $[N_2] = 7.6 \cdot 10^{18}$ molecules·cm^{-3}, and $[O_2] = 1.75 \cdot 10^{18}$ molecules·cm^{-3}. Thus, all major species concentrations are two to four orders of magnitude higher than the HO_2 concentration, and thereby also the oxygen atom concentration, which means that reactions (1) to (4) can be treated with pseudo-first-order kinetics. The OH production, [OH], as a function of time, t, can be written:

$$[OH](t) = [OH]_0 \left\{ 1 + \frac{k_0}{k_{eff}} \left(1 - e^{-k_{eff}t} \right) \right\} \tag{5}$$

where $[OH]_0$ is the initial OH concentration and the expressions for k_0 corresponding to $O(^1D)$ and $O(^3P)$, respectively, are given by

$$k_0^P = 2k_1^P[H_2O] + k_2^P[CH_4] \quad \text{for } O(^3P) \tag{6P}$$

$$k_0^D = 2k_1^D[H_2O] + k_2^D[CH_4] \quad \text{for } O(^1D) \tag{6D}$$

whereas the corresponding expressions for k_{eff} are

$$k_{eff}^P = k_1^P[H_2O] + k_2^P[CH_4] \quad \text{for } O(^3P) \tag{7P}$$

$$k_{eff}^D = k_1^D[H_2O] + k_2^D[CH_4] + k_3[N_2] + k_4[O_2] \quad \text{for } O(^1D) \tag{7D}$$

Rate constants for reactions (1) to (4), found in the literature, are given in Table 1.

Table 1 Reaction rate constants, for reactions (1) to (4), used to estimate the OH production originating from oxygen atoms produced by HO_2 photolysis. Rate constants are in units of $cm^3 molecule^{-1}s^{-1}$.

Rate constant	Oxygen state	Value	Temp. (K)	Reference
k_1^D	$O(^1D)$	$2.1 \cdot 10^{-10}$	295	Takahashi et al. [33]
k_1^P	$O(^3P)$	$5.6 \cdot 10^{-14}$	1200	Lifshitz & Michel [34]
k_2^D	$O(^1D)$	$1.9 \cdot 10^{-10}$	227-450	Vranckx et al. [35]
k_2^P	$O(^3P)$	$2.1 \cdot 10^{-12}$	1200	Baulch et al. [36]
k_3	$O(^1D)$	$2.4 \cdot 10^{-11}$	1200	Blitz et al. [37]
k_4	$O(^1D)$	$3.8 \cdot 10^{-11}$	295	Blitz et al. [37]

As can be seen in Table 1, the rate constants for $O(^1D)$ reactions are several orders of magnitude higher than the corresponding rate constants for $O(^3P)$ reactions. Calculation of k_0^P and k_{eff}^P based on the reaction rate constants given in the table and the aforementioned major species concentrations gives the following values: $k_0^P = 1.61 \cdot 10^6$ s^{-1} and $k_{eff}^P = 1.59 \cdot 10^6$ s^{-1}. Thus $k_0^P/k_{eff}^P \approx 1$, which means that expression (5) may be simplified into

$$[OH](t) = [OH]_0 \left(2 - e^{-k_{eff}^P t} \right) \tag{8P}$$

for $O(^3P)$ kinetics. For $O(^1D)$ Equation (5) should be written:

$$[OH](t) = [OH]_0 \left\{ 1 + \frac{k_0^D}{k_{eff}^D} \left(1 - e^{-k_{eff}^D t} \right) \right\} \tag{8D}$$

Here $k_0^D = 3.1 \cdot 10^8$ s^{-1} and $k_{eff}^D = 4.9 \cdot 10^8$ s^{-1}, i.e. $k_0^D/k_{eff}^D = 0.63$. The fact that $k_{eff}^D/k_{eff}^P = 310$ reveals that the OH production rate for $O(^1D)$ kinetics is predicted to be more than two orders of magnitude faster than for $O(^3P)$ kinetics.

Assuming that only OH and $O(^1D)$ are formed upon HO_2 photolysis, i.e. $[O(^1D)]_0 = [OH]_0$, then the production of $O(^3P)$, via reactions (3) and (4), as a function of time can be written:

$$[O(^3P)](t) = \frac{k'}{k_{eff}^D} \left(1 - e^{-k_{eff}^D t} \right) [OH]_0 \tag{9}$$

where

12

$$k' = k_3[N_2] + k_4[O_2]$$

Using rate constants from Table 1 and the same concentrations as before results in $k'/k_{eff}^D = 0.51$. Now, Equations (8D) and (9) show that the OH/O(^{3}P) branching ratio is 1.63/0.51 = 3.2, which means that additional OH production via O(^{3}P) reactions cannot be neglected even if all oxygen atoms are formed in the ^{1}D state. The additional OH production is given by the following expression:

$$[OH](t) = [O(^3P)](t) \cdot (1 - e^{-k_2't}) = \frac{k'}{k_{eff}^D}\left(1 - e^{-k_{eff}^D t}\right)\left(1 - e^{-k_2't}\right)[OH]_0 \quad (10)$$

where

$$k_2' = k_2^P[CH_4]$$

It is now possible to formulate a general expression for photochemical OH production in the reaction zone by combining Equation (8P), corresponding to OH production from directly formed O(^{3}P), Equation (8D), corresponding to OH production from directly formed O(^{1}D), and Equation (10), representing OH production through O(^{3}P) formed by deactivation of O(^{1}D). We introduce the variable x ($0 \leq x \leq 1$), designating the O(^{1}D)/O(^{3}P) branching ratio, i.e. x = 0 corresponds to 0% O(^{1}D) and 100% O(^{3}P). The full expression, with rate constants inserted, then becomes:

$$\frac{[OH](t)}{[OH]_0} = (1 - x)\left(2 - e^{-k_{eff}^P t}\right) + x\left\{\left[1 + \frac{k_0^D}{k_{eff}^D}\left(1 - e^{-k_{eff}^D t}\right)\right] + \right.$$

$$\left. \frac{k'}{k_{eff}^D}\left(1 - e^{-k_{eff}^D t}\right)\left(1 - e^{-k_2't}\right)\right\} \quad (11)$$

With values on rate constants (in the unit ns^{-1}) inserted, the equation becomes

$$\frac{[OH](t)}{[OH]_0} = (1 - x)(2 - e^{-0.0016t}) + x\{[1 + 0.63(1 - e^{-0.49t})] + 0.52(1 -$$

$$e^{-0.49t})(1 - e^{-0.0016t})\} \quad (12)$$

Consumption of OH has been neglected in the model. A calculation taking the major OH-consumption channel into account, i.e. $OH + CH_4 \rightarrow H_2O + CH_3$ ($k = 1.70 \cdot 10^{-12}$ $cm^3 molecule^{-1} s^{-1}$ [38]), shows that inclusion of this channel changes the OH concentration by less than 13% at the time 200 ns. In the present study we are only interested in times shorter than 200 ns, and in particular the initial 10 ns following HO_2 photolysis, where the error is estimated to be less than 1%, and thus neglecting OH consumption in the model is justified.

4. Results and discussion

4.1 Excitation spectra of OH fragments recorded in a CH$_4$/air flame

Picosecond-PFLIF excitation spectra recorded in the reaction zone of a laminar CH$_4$/air flame were studied. Johansson et al. have previously estimated that 87% of the integrated reaction zone signal in PFLIF experiments in the investigated flame is due to OH-fragments from HO_2, about 12% from H_2O_2 and the remaining 1% most likely from CH_3O_2 [27]. The fragment signal is thus strongly dominated by fluorescence from OH created by HO_2 photolysis. Figure 2 shows OH fragment excitation spectra for three different pump-probe delay times, namely 0.5, 2.0 and 5.0 ns, together with a spectrum recorded without firing the photolysis laser, i.e. a spectrum corresponding to the naturally present OH in the reaction zone. To facilitate comparison of the spectral shapes, the spectra are normalized to the intensity of the strongest peak, which is situated at 283.0 nm and corresponds to $Q_2(1,2,3)$, forming a bandhead that overlaps with $Q_1(6)$. The normalized spectra allow investigation of how the rotational population distribution of the created OH fragments varies with pump-probe delay as it is reflected through the relative strengths of the spectral peaks.

As can be seen in Fig. 2, overall the shapes of the spectra appear rather similar. However, a closer look reveals some differences; for example, the relative intensity of the peak at 284.0 nm, corresponding to the overlapping $Q_1(9)$ and $Q_2(8)$ transitions, is clearly higher in the

14

spectrum recorded at 5.0 ns pump-probe delay, shown in panel (c), than in the spectra recorded at 0.5 (a) and 2.0 ns (b) delay. Similarly, the peak at 283.3 nm, corresponding to the overlapping $Q_1(7)$ and $Q_2(5)$ transitions, is higher in the spectrum recorded at 5.0 ns delay (c) than in the spectra recorded at 0.5 (a) and 2.0 ns (b) delay. These observations suggest that the spectrum recorded at 0.5 ns delay (a) reflects a cooler rotational population distribution than the spectrum recorded at 5.0 ns delay (c).
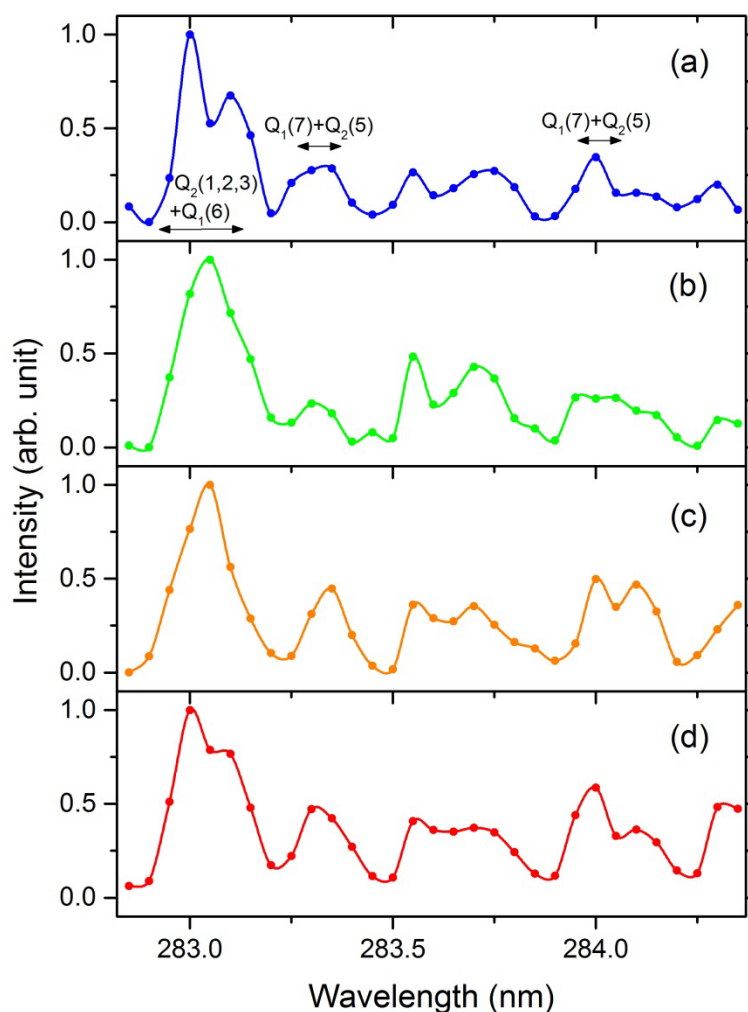

Fig. 2 Excitation spectra recorded in the reaction zone of the flame. (a), (b), and (c) show OH fragment spectra recorded at the pump-probe delays 0.5, 2.0, and 5.0 ns delay, respectively, while panel (d) displays an OH spectrum recorded without a preceding photolysis pulse, thus reflecting naturally present OH in the reaction zone.

Furthermore, the spectrum recorded at 5.0 ns delay (c) agrees fairly well with the spectrum recorded for naturally present OH, i.e. the thermal spectrum shown in (d). The sum-of-squares difference between each fragment spectrum (a, b, and c) and the thermal spectrum (d) were calculated using the expression $SSQ = \frac{1}{N-1}\sum_i^N\left(I_i - I_i^{thermal}\right)^2$, where N is the number of data points (31), I_i is the intensity corresponding to data point i in the spectrum, and $I_i^{thermal}$ is the intensity corresponding to data point i in the thermal spectrum. The following results were obtained: SSQ = 0.029 (a), 0.026 (b), and 0.016 (c), underlining that the spectrum recorded at 5.0 ns (c) delay best matches the natural OH spectrum (d).

Sinha et al. found that most of the available energy disposal resulting from 220 nm photolysis of HO_2 ends up as internal energy in the oxygen atom and that almost none (1.7%) of the available energy is transferred into vibrational and rotational energy in the OH fragment [29]. Thus, the nascent OH fragments are vibrationally and rotationally cold. An excitation spectrum based on the nascent rotational population distribution measured by Sinha et al. [29] was simulated and compared to our spectrum recorded at a pump-probe delay of 0.5 ns, as shown in Fig. 3. Overall, the two spectra have similar shapes, dominated by the double-peak at 283.0-283.1 nm, corresponding to transitions originating in low-energy rotational states, while the other peaks, corresponding to transitions mainly stemming from higher rotational states, are all below 35% of the intensity of the highest peak. There are minor differences between the two spectra, which is not surprising as they correspond to somewhat different photolysis wavelengths (266 nm for our experiment and 220 nm for the experiment by Sinha et al.) and the fact that our spectrum is acquired at 0.5 ns pump-probe delay, during which some rotational relaxation certainly has occurred, while the results reported by Sinha et al. are for truly nascent fragments, i.e. zero delay.
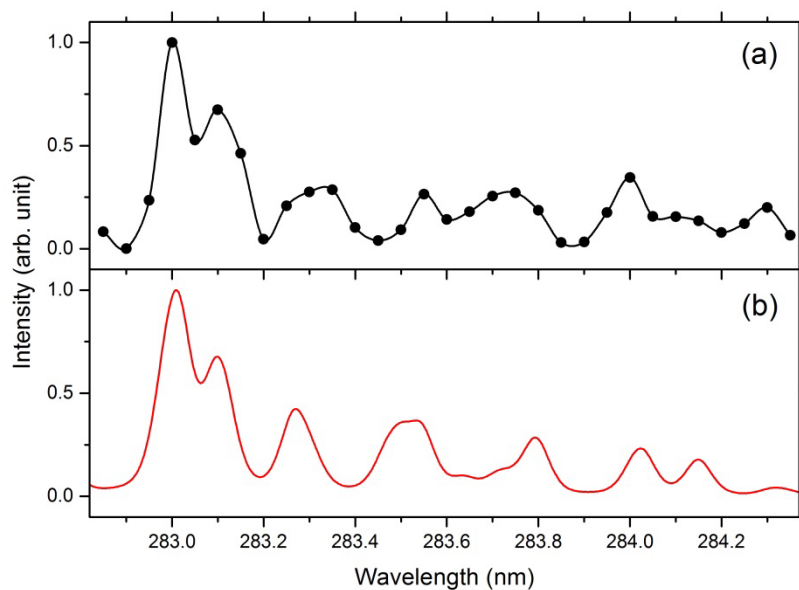
Fig. 3 (a) OH fragment excitation spectrum recorded with 0.5 ns pump-probe delay in the reaction zone of the flame and, (b) a simulated excitation spectrum based on the nascent rotational distribution measured for 220-nm photolysis of HO_2 by Sinha et al. [39].

The analysis of the excitation spectra recorded in the reaction zone of the stoichiometric CH_4/air flame hence suggests that the population distribution of the nascent OH fragments is rotationally cold and similar to the nascent distribution resulting from HO_2 photolysis previously measured by Sinha et al [29]. Furthermore, the results indicate that it takes on the order of 5 ns for the non-equilibrium nascent rotational distribution to relax into a thermal distribution.

4.2 OH fragment emission spectra recorded at different pump-probe delays in the flame

Spectrally resolved ps-PFLIF spectra were recorded with the probe laser tuned to 283.0 nm, i.e. the strongest peak in the spectra shown in Fig. 2. Having the spectrograph oriented so that its entrance slit is horizontal allows acquisition of spectrally dispersed fluorescence along a horizontal line through the flame, defined by the focused probe laser beam, i.e. the resulting image on the CCD camera has the spectral scale on the horizontal axis and radial position in

17

the flame on the vertical axis. Measurements were undertaken at six different pump-probe delay times, ranging from 0.5 ns to 22.5 ns. Figure 4 shows the result obtained with a delay of 4.0 ns. Panel (a) shows the spectral image with wavelength along the horizontal axis, radial distance along the vertical axis, and the color reflects the relative signal intensity as defined by the color bar to the right. The different combustion zones are defined as follows; the unburnt zone is situated between -0.5 and 0.5 mm, the reaction-zone signal covers the range 0.5 to 1.5 mm, and the product-zone signal ranges from 1.5 to 2.25 mm. By integrating the signal along the vertical direction in each zone, the average spectrum in each zone was extracted, and these spectra are displayed in panels (b)-(d).
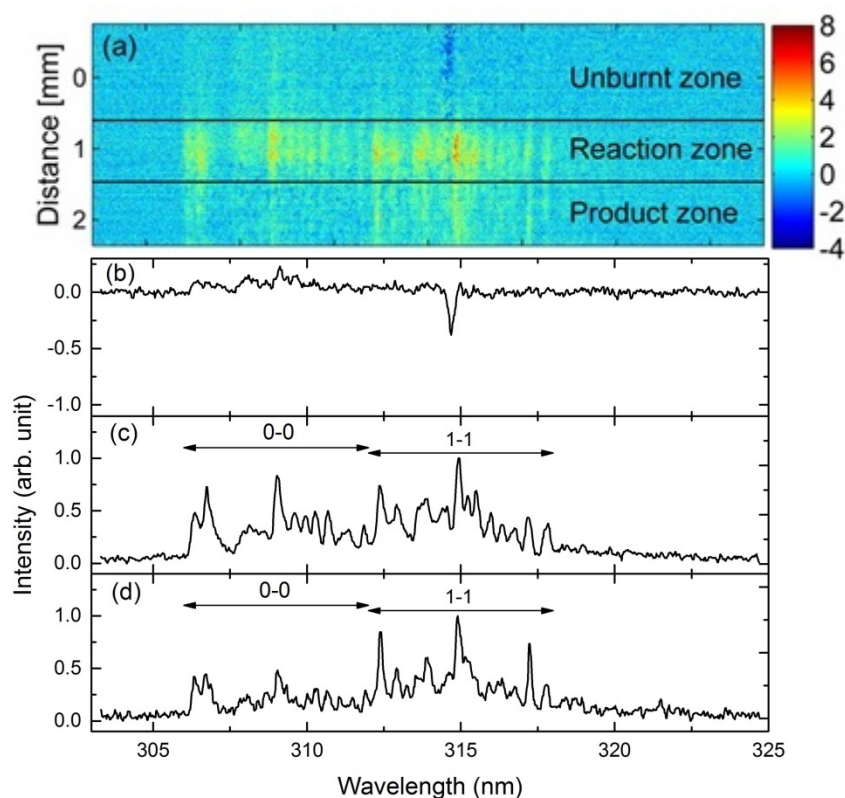

Fig. 4 (a) Spectral PFLIF image recorded in a stoichiometric CH_4/air flame with a pump-probe delay time of 4 ns. Integration along the radial axis within the different zones, indicated by the solid lines in (a), results in the spectra shown in panels (b)-(d), where (b) corresponds to the unburnt zone, (c) the reaction zone, and (d) the product zone.

The signal in the spectrum corresponding to the unburnt zone, shown in (b), is essentially zero throughout the entire spectral range, except the negative peak at around 315 nm. It has been found that the pump pulse dissociates methane and produce excited CH fragments, emitting fluorescence via the $C^2\Sigma^+$-$X^2\Pi$ transition near 315 nm [40, 41]. Although this emission should be canceled through subtraction, it is possible that the probe pulse dissociates or photoionizes some of the produced CH*, and then a negative net signal near 315 nm should appear.

The spectral positions of the peaks in the reaction-zone and product-zone spectrum, shown in (c) and (d), respectively, prove that the emission in these zones is LIF from OH fragments. The signal in the reaction zone stems from HO_2 photolysis. As already alluded to in the introduction, it is known from previous work that OH can be produced photochemically in the product zone via photolysis of CO_2, whereupon the produced oxygen atoms react with H_2O or H_2 forming OH [27], which most likely is the mechanism behind the OH signal observed in the product zone. Both the reaction zone spectrum (panel c) and the product zone spectrum (panel d) exhibit stronger emission in the 1-1 vibrational band (band origin at 314.2 nm) than in the 0-0 vibrational band (band origin at 308.9 nm), which most likely is due to the very high fluence of the probe laser (~3 GW/cm^2), inducing strong photoionization out of the pumped v' = 1 vibrational state. In such a case the photoionization rate might be significantly larger than the collisional quenching and vibrational energy transfer (VET) rates, leaving most of the population in the v' = 1 state during the course of the short-lived fluorescence. The wealth of rotational structure in the spectra suggests that the rotational energy transfer (RET) rates are high enough to redistribute the population from the directly pumped rotational states to a large number of rotational states.

As is evident from the color-coded intensity scale in panel (a) at 4.0 ns pump-probe delay the product-zone signal is significantly weaker than the signal of interest, i.e. the OH fragment

fluorescence in the reaction zone. Overall, the spectral shapes of the reaction-zone (panel c) and the product-zone spectrum (panel d) are fairly similar. However, the relative intensity of the 1-1 band versus the 0-0 band is somewhat higher in the product-zone spectrum than in the reaction-zone spectrum. Comparison with simulated (LIFBASE [42]) OH(A-X) emission spectra reveals that the best-fit for the reaction-zone spectrum is obtained with 38% of the population in $v' = 0$ and 62% in $v' = 1$, whereas the corresponding values for the product-zone spectrum are 25% in $v' = 0$ and 75% in $v' = 1$. The reason for this difference is difficult to specify since the photoionization rate is critically dependent on the spatial probe laser profile, which was neither a top-hat nor a smooth Gaussian.

4.3 OH fragment signals recorded at different pump-probe delays

Radial profiles were extracted from spectral images recorded at different pump-probe delays (Fig. 4(a) shows the spectral image acquired for 4-ns delay) by integrating the signal in the regions 306-314 nm and 316-320 nm, which were chosen to avoid the negative signal contribution in the unburned zone near 315 nm (see Fig. 4(b)), and Fig. 5 shows the resulting signal profiles.
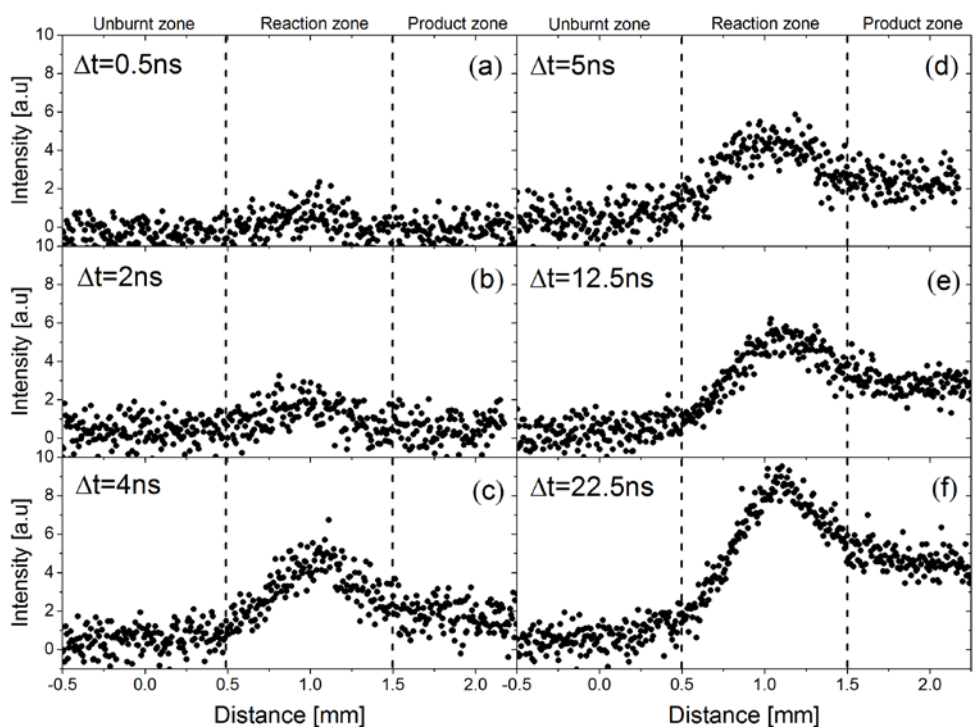
Fig. 5 PFLIF signal profiles recorded at six different pump-probe delays (0.5-22.5 ns).

As expected, the signal in the unburnt zone is close to zero for all investigated pump-probe delays. For the two shortest delays, OH fluorescence is only present in the reaction zone, as shown in panel (a) and (b). At 4.0 ns delay, i.e. panel (c), the photochemically produced OH signal starts to get discernable in the product zone. This signal is then increasing with increasing pump-probe delay, as evident from panel (c) to (f).

4.3.1 Analysis of the product-zone signal

The product-zone signal, taken as the average signal between 1.75 and 2.0 mm in Fig. 5, is plotted versus pump-probe delay in Fig. 6. The square symbols designate our results, while the circles are results by Johansson et al. [27], who performed a similar study in the same flame, using the same laser wavelengths but with laser pulses of 5-ns duration. The solid line is an OH-production curve calculated by Johansson et al. assuming that 10% of the CO_2 molecules are photodissociated into CO and $O(^3P)$ [27]. The initial OH-production gradient

indicated by our data is ~3.5 times steeper than the initial slope of the curve calculated by Johansson et al. One possible reason for this difference could be that the photodissociation quantum yield was higher in the present experiment (25%) than the value used in the calculation by Johansson et al. (10%). The current photolysis yield was calculated following Equation (1) in [27], using a photolysis-laser pulse energy of 5 mJ, a laser-beam cross section area of $1.5 \cdot 10^{-4}$ cm^2, and a CO_2 absorption cross section of $6.0 \cdot 10^{-21}$ cm^2 [27, 43]. It is also possible that a small amount of $O(^1D)$ was formed in the present CO_2 photolysis, and the OH-buildup through reaction with H_2O would then be significantly faster due to the considerably larger rate constant for $O(^1D)$ than for $O(^3P)$, as can be seen in Table 1 in Section 3. Due to the relatively high oxygen atom concentration produced by 25% CO_2 photolysis, pseudo-first-order kinetics is not applicable, wherefore we refrain from estimating any value on the $O(^1D)/O(^3P)$ branching ratio for the present CO_2 photolysis.
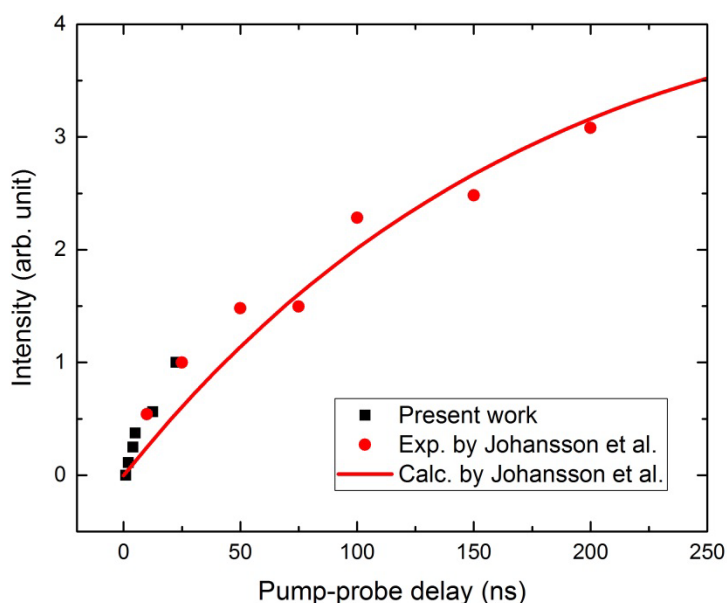

Fig. 6 Product-zone signals versus pump-probe delay. The squares designate data recorded in the present study, the circles indicate experimental data recorded in the same flame by Johansson et al. [27], and the solid line is a chemical-kinetic calculation of OH production from Johansson et al. [27].

4.3.2 Analysis of the reaction-zone signal

From the data shown in Fig. 5, the peak intensity in the reaction zone was extracted for each pump-probe delay. Given that the flame was not one-dimensional, but rather had a circular cross section if cut in a horizontal plane, the curvature of the flame together with the widths of the laser beams caused the signal in the product zone to "bleed" into the reaction zone. To compensate for this effect, the average signal intensity between 2.0 and 2.2 mm was subtracted from the reaction-zone peak intensity for each pump-probe delay. The resulting reaction-zone signal versus pump-probe delay is shown in Fig. 7(a). Although the data points are somewhat scattered, which is mainly due to difficulties in maintaining identical spatial overlap of the pump and probe laser beams as the delay between the two laser pulses are changed using the optical delay line (see Fig. 1), Fig. 7(a) clearly shows that the signal in the reaction zone is increasing with increasing pump-probe delay.
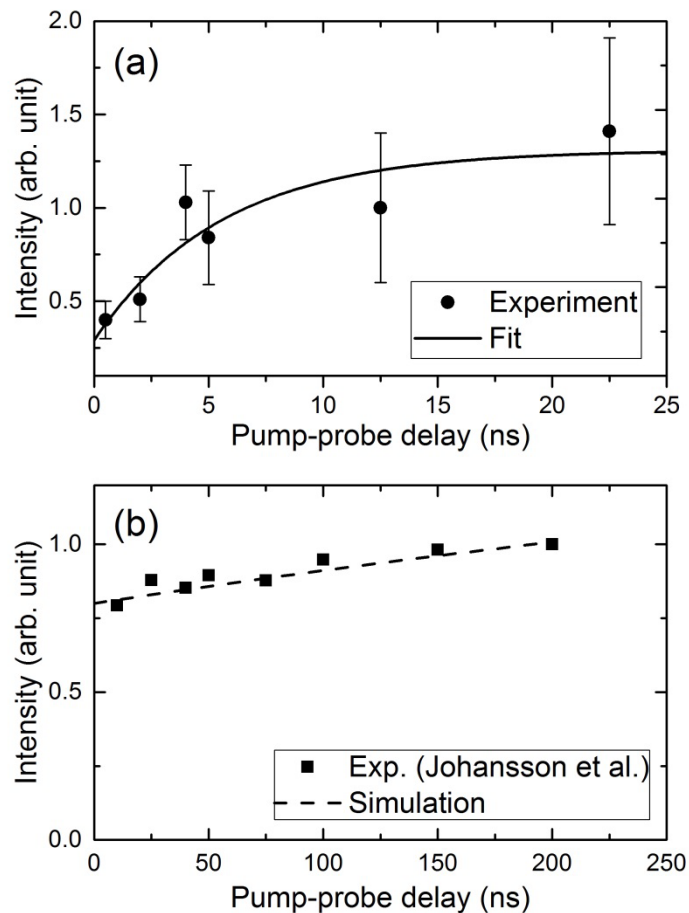
Fig. 7 Reaction-zone signal intensities vs pump-probe delay. Panel (a) shows our experimental data (symbols) together with a fit (solid line). Panel (b) shows the result obtained in the same flame by Johansson et al. [27], using identical laser wavelengths but with two orders of magnitude lower photolysis laser intensity. The dashed line in (b) is OH production simulated using Equation (12) with x = 0 and $[OH]_0 = 0.8$. Note the different time scales in (a) and (b).

The signal growth rate is highest initially and then decreases with increasing delay. For the four shortest pump-probe delays (0.5-5.0 ns), the results reported in Section 4.1 show that the rotational population distribution of the OH fragment is non-thermal in this temporal regions, which suggests that the early signal increase, to some extent, might be due to rotational energy transfer processes. However, LIFBASE simulations [42] based on the

nascent rotational population distribution measured by Sinha et al. [29] and a thermal distribution corresponding to 1000 K suggest that the signal growth due to population transfer should be only 20%. An exponential function of the form $I(t) = I_0 - Ae^{(-kt)}$ was fitted to the data points (solid line in Fig. 7(a)), resulting in the following best-fit parameters: $I_0 = 1.31$ (0.38), $A = 1.02$ (0.36) and $k = 1.8 \cdot 10^8$ ($1.3 \cdot 10^8$) s^{-1}, where the numbers in brackets are standard errors. Although, there is deviation between the data points and the fitted curve, the fit suggests that the OH concentration grows very rapidly during the first 5 ns. The fitted rate constant, $k = 1.8 \cdot 10^8$ s^{-1}, should be a valid order-of-magnitude estimate of the effective OH production rate in the reaction zone.

Just like for the product-zone signal discussed in the previous Section (4.3.1), it is interesting to compare the temporal development of the reaction-zone signal observed in the present study (Fig. 7(a)) with the corresponding result obtained by Johansson et al. [27], which is indicated by the square symbols in Fig. 7(b). Both the present data and the result obtained by Johansson et al. show that the OH signal increases with increasing pump-probe delay. However, in contrast to the present result (panel a), there is no sign of an initial steep gradient in the data recorded by Johansson et al. (panel b). The lack of this feature might of course be due to the fact that there are no data points for pump-probe delays shorter than 10 ns in the data by Johansson et al. It is, however, clear that an increase in OH signal with increasing pump-probe delay is expected since oxygen atoms produced by HO_2 photolysis can form OH through reactions with any hydrogen-containing species present in the reaction zone. A steep initial gradient is expected if a fraction of the produced oxygen atoms ends up in the excited ^1D state, which indeed is observed in the present result (Fig. 7(a)). However, if all oxygen atoms are formed in the ^3P ground state a much slower OH production is expected, which seems to be the case for the data recorded by Johansson et al. (Fig. 7(b)). Production of

OH through oxygen atoms formed by HO_2 photolysis will be discussed in the following section.

4.4 Production of OH in the reaction zone through oxygen-atom chemistry

Figure 8 shows OH-production curves calculated with Equation (12) for the $O(^1D)/O(^3P)$ branching ratios x = 0, 0.2, 0.4, 0.6, 0.8, and 1.0. As can be seen, the presence of $O(^1D)$ is manifested mainly through a steep initial slope. However, the character of the curve beyond 10 ns is also influenced by the $O(^1D)$ content; the relative increase in OH concentration from 10 to 200 ns is decreasing with increasing x. In that region, the OH concentration is increasing by the following percentages for the different branching ratios: 25.2% (x = 0), 20.3% (x = 0.2), 16.4% (x = 0.4), 13.2% (x = 0.6), 10.5% (x = 0.8), and 8.2% (x = 1.0). This dependence can thus also be used to estimate the $O(^1D)/O(^3P)$ branching ratio. Figure 7(b), displaying the data recorded by Johansson et al. [27], shows that the OH signal increases by 24±2 % from 10 ns to 200 ns. This growth agrees well with the 25.2% predicted by the model for x = 0 (solid black curve in Fig. 8), strongly supporting that the HO_2 photolysis in the experiments by Johansson et al., which were performed with nanosecond laser pulses, only produced ground-state oxygen atoms, i.e. $O(^3P)$.

Even though the scattering of the data points acquired in the present experiment, shown in Fig. 7(a), prevents a precise quantitative determination of the $O(^1D)/O(^3P)$ branching ratio, the very large rate constant found by the fit (solid line in Fig. 7(a)), i.e. $1.8 \cdot 10^8$ s^{-1}, suggests a significant $O(^1D)$ production yield. The time-derivative at time zero as a function of the branching ratio, x, can be determined using Eq. (12). The derivatives corresponding to six curves displayed in Fig. 8 are: 0.0016 (x = 0), 0.06 (x = 0.2), 0.12 (x = 0.4), 0.19 (x = 0.6), 0.25 (x = 0.8), and 0.31 ns^{-1} (x = 1). The corresponding measured derivative is determined from the fit to the experimental data, i.e. the solid line in Fig. 7(a), which results in the value

26

0.18 ($\pm$0.13) ns^{-1}. Thus, our results with picosecond laser photolysis suggest that $0.2 \leq x \leq 1$, i.e. at least 20% of the oxygen atoms are formed in the excited ^{1}D state. The fit to the data shown in Fig. 7(a) indicates that the OH signal increases by a factor 4 between 0 and 22.5 ns. As can be seen in Fig. 8, the corresponding ratio increases with x, and the highest ratio, obtained for $x = 1$, is 1.65. Thus, the experimental ratio is higher than the maximum ratio predicted by the model, although a branching ratio of 1.0 lies within the uncertainty of the experimental data (accounting for the standard errors of the fit indicates that the ratio can be as low as 1.5). This observation suggest that the branching ratio should be close to unity, but since the data points are quite scattered and the number of data points are small we stand by the conclusion that at least 20% of the oxygen atoms are formed in the excited ^{1}D state. This result is hence different from the previously discussed result obtained with nanosecond laser photolysis, for which only O(^{3}D) production is indicated, which will be further discussed in the next section.
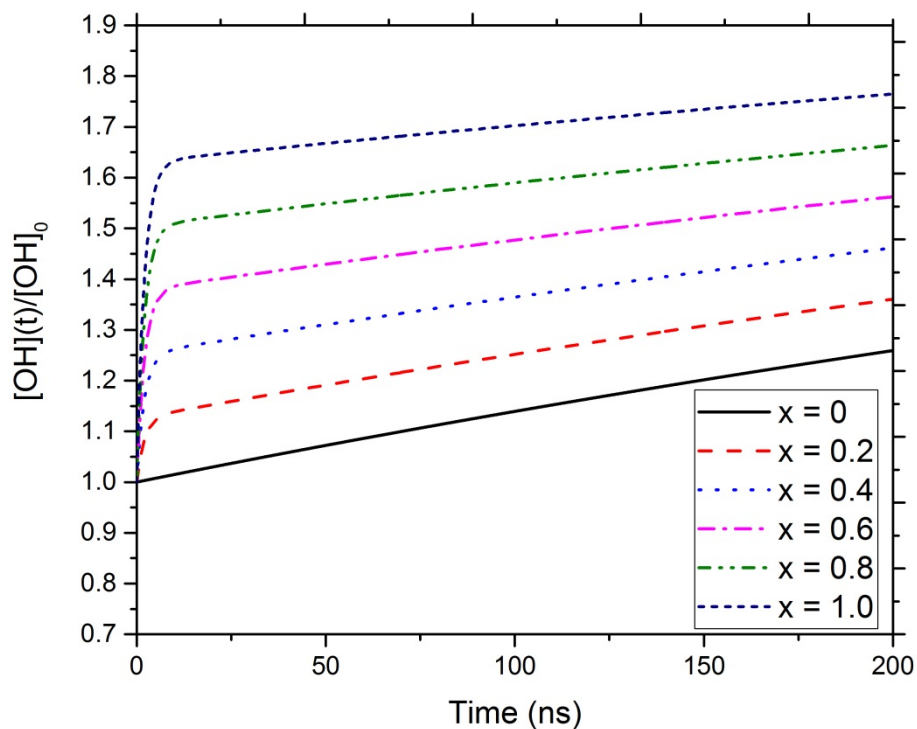
Fig. 8 OH production calculated using Equation (12) for various $O(^1D)/O(^3P)$ branching ratios, x (x = 0 means that only $O(^3P)$ is formed, while x = 1 means that only $O(^1D)$ is formed). It is notable that already a 20% $O(^1D)$ production shows up as a distinct initial rapid signal rise feature (red dashed line).

4.5 Discussion of differences in HO₂ photolysis with picosecond and nanosecond laser photolysis

Based on heat of formation data [44, 45], the energy required to dissociate HO_2 into O and OH fragments is 2.76 eV. A single 266-nm photon corresponds to 4.66 eV, and this energy is more than enough to dissociate the molecule. An excess energy of 1.90 eV is thus available for distribution among the O and OH products. Excitation of the oxygen atom to its ^1D state requires 1.95 eV, and thus the available energy is not high enough to form $O(^1D)$ using single-photon photodissociation with 266-nm light. This fact is supported by the result of the nanosecond laser experiment [27], suggesting zero $O(^1D)$ production, but not by our picosecond laser experiment, which indicates that more than 20% of the produced oxygen atoms are in the ^1D state. A plausible explanation of the discrepancy between the two results is that the picosecond laser pulses might cause 2-photon photodissociation. The irradiance of the 80-ps photolysis laser pulses used in the present study was ~400 GW/cm^2 while it was 2.5 GW/cm^2 for the 5-ns laser pulses used by Johansson et al. [27]. These numbers indicate that the probability for 2-photon absorption is about four orders of magnitude higher in the present study than in the experiments by Johansson et al. Multi-photon photodissociation of CH_4 has been observed with similar laser irradiance as the one used in the present study [41].

With the energy corresponding to two 266-nm photons (9.32 eV) available, the excess energy becomes 6.56 eV, which definitely is sufficient to excite the oxygen fragment into its ^1D state. In fact, this excess energy in principle also allows production of $OH(A^2\Sigma^+)$.

Spectrally resolved emission observed with only the photolysis laser fired (not shown) indicates a weak OH fluorescence signal. However, the spatial distribution of this signal does not show a peak in the reaction zone, but rather a profile reflecting the distribution of natural OH in the flame. Given the relatively broad linewidth of the picosecond laser pulse (~ 5 cm^{-1}, FWHM), it is possible to excite OH using weak vibronic transitions in the vicinity of 266.0 nm [46], which thus may be the origin of the observed weak OH fluorescence.

4.6 Diagnostic implications

In terms of HO$_2$ diagnostics through PFLIF, i.e. photodissociation followed by OH fragment detection with LIF, the present study, performed in a premixed stoichiometric CH$_4$/air flame, shows that it is possible to virtually eliminate the product-zone interference, due to photochemically produced OH, by using 80-ps laser pulses and a pump-probe delay time shorter than 4 ns, as shown in Fig. 5. However, the high irradiance of the picosecond photolysis pulses induces prompt emission, which has not completely vanished for pump-probe delays shorter than 5 ns, and therefore this background signal must be subtracted. Furthermore, it is found that the signal-of-interest, i.e. the OH fragment fluorescence stemming from HO$_2$ in the reaction zone, increases rapidly with increasing pump-probe delay, mainly due to very fast OH production through O(^{1}D) + CH$_4$ $\rightarrow$ OH + CH$_3$. Thus, using high-intensity picosecond laser pulses results in a photochemical interference whose magnitude is strongly dependent on the pump-probe delay time. The result obtained with the shortest pump-probe delay investigated, i.e. 0.5 ns, shown in Fig. 5(a), exhibits a signal-to-noise ratio of 2, which indicates that decreasing the pulse energy, in order to reduce the production of O(^{1}D) by 2-photon photodissociation, is not a viable alternative for studies in the present flame, as the signal-to-noise ratio then becomes too low. Although beneficial in terms of reducing photochemical interferences, using pump-probe delays shorter than 5 ns implies OH

fragments with non-thermal rotational distributions, which complicates quantification of the results.

An analysis of PFLIF measurements performed in the same flame by Johansson et al. [27], shows that photochemical OH production occurs in the reaction zone also when nanosecond laser pulses are used. However, our OH-production analysis suggests that no $O(^1D)$, but only $O(^3P)$, is formed upon HO_2 photolysis with the moderate irradiance used by Johansson et al., the photochemical OH production is at least two orders of magnitude slower than for the high-intensity picosecond laser photolysis used in the present work. Equation 12 with x = 0, i.e. the solid black line in Fig. 8, shows that the signal contribution due to photochemically produced OH is only 1.5% of the nascent OH fragment concentration for a pump-probe delay of 10 ns. Thus, we conclude that PFLIF using nanosecond laser pulses can be performed for HO_2 detection in premixed CH_4/air flames with negligible photochemical interference in the reaction zone. However, the photochemical interference in the product zone cannot be eliminated, which is possible with picosecond pulses, as can be seen in Fig. 5.

Our overall conclusion in terms of flame diagnostics with PFLIF is that a setup based on nanosecond laser pulses, rather than picosecond pulses, appears preferable, since photochemical OH production originating from the HO_2 photolysis can be avoided and the photochemical interference in the product zone, stemming from CO_2 photolysis, can be minimized using the shortest possible pump-probe delay. In order to avoid the risk of probing non-thermal OH fragments, the pump-probe delay should not be shorter than 10 ns if laser pulses of 5 ns duration are used. It should however be emphasized that the optimum choice, nanosecond or picosecond PFLIF, is dependent on the flame chemistry, which varies with fuel and stoichiometry. Thus, for application in an arbitrary flame, the experimental setup should, if possible, be selected based on predictions from chemical kinetics modelling. Although an investigation of the capacity of the method for various flames is outside the scope of the

30

present work, it should be noted that the production of O(^{1}D) through 2-photon dissociation rapidly decreases with decreasing pump laser irradiance. Hence, for flames containing higher concentrations of hydrogen peroxides, it might be possible to use picosecond pulses of lower irradiance while obtaining adequate signal-to-noise ratio and suppression of the product-zone interference. Picosecond studies would be particularly attractive for flames where the H_2O_2 concentration strongly exceeds the HO_2 concentration, since production of two OH fragments is a very dominant channel in H_2O_2 dissociation [47]. An experimental and modelling study performed by Rodriguez et al. [48] shows that the low-temperature oxidation of dimethyl ether (DME) yields significantly higher concentrations of H_2O_2 than HO_2. This finding indicates that ps-PFLIF might be a better alternative than ns-PFLIF for studies of hydrogen peroxide in DME flames.

5. Conclusions

Photofragmentation laser-induced fluorescence (PFLIF) was for the first time performed with picosecond laser pulses for detection of hydroperoxyl radicals (HO_2) in a stoichiometric laminar methane/air flame. Photofragmentation is performed with a pump laser pulse of 80 ps duration and a wavelength of 266 nm, whereupon the produced OH photofragments are detected by a second 80-ps probe laser pulse, inducing fluorescence via excitation in the $A^2\Sigma^+(v=1) \leftarrow X^2\Pi(v=0)$ band of OH near 283 nm. Excitation spectra of OH photofragments formed in the reaction zone suggest that the population distribution of the nascent OH fragments is rotationally cold and that it takes on the order of 5 ns for the nascent non-equilibrium rotational distribution to relax into a thermal distribution. Photochemical OH production was observed both in the reaction zone and the product zone of the flame. Comparison with a kinetic model for OH production suggests that more than 20% of the oxygen fragments produced in the reaction zone are formed in the excited ^{1}D state, which

explains the very rapid initial signal growth observed. The OH-production model was also compared with previous reaction-zone data, acquired with nanosecond laser pulses in the same flame, indicating that only ground-state (^{3}P) oxygen atoms are formed. The clear difference between the two results is most likely due to the fact that the picosecond pulses, having more than two-orders of magnitude higher irradiance than the nanosecond pulses used in the previous study, may cause 2-photon photodissociation, which allows O(^{1}D) to be produced. In terms of flame diagnostics with PFLIF, it is concluded that a setup based on nanosecond laser pulses, rather than picosecond pulses, appears preferable, since photochemical OH production in the reaction zone can be avoided and the photochemical interference in the product zone, stemming from CO_2 photolysis, can be minimized by using as short pump-probe delay as possible. However, in terms of applications in other flames, it is noted that it might be possible to use picosecond pulses of significantly lower irradiance, given that the flame contains a significantly higher concentration of hydrogen peroxides. In such cases picosecond pulses together with a short pump-probe delay, could potentially allow efficient suppression of the product-zone interference while still obtaining adequate signal-to-noise ratio. In particular, picosecond studies appear attractive for flames containing H_2O_2 at a concentration that strongly exceeds the HO_2 concentration, since the production yield of oxygen atoms is much lower for H_2O_2 than for HO_2.

Acknowledgement

References

[1] J.A. Logan, M.J. Prather, S.C. Wofsy, M.B. McElroy, Tropospheric chemistry: A global perspective, J. Geophys. Res.-Oceans 86 (1981) 7210-7254.

[2] M. Lee, B.G. Heikes, D.W. O'Sullivan, Hydrogen peroxide and organic hydroperoxide in the troposphere: a review, Atmos. Environ. 34 (2000) 3475-3494.

[3] K.C. Salooja, The degenerate chain braching intermediate in hydrocarbon combustion: Some evidence from studies on the isomeric hexanes, Combust. Flame 9 (1965) 219-227.

[4] J.V. Michael, J.W. Sutherland, L.B. Harding, A.F. Wagner, Initiation in H_2/O_2: Rate constants for $H_2+O_2 \rightarrow H+HO_2$ at high temperature, Proc. Combust. Inst. 28 (2000) 1471-1478.

[5] W.J. Pitz, C.K. Westbrook, Chemical kinetics of the high pressure oxidation of n-butane and its relation to engine knock, Combust. Flame 63 (1986) 113-133.

[6] C.K. Westbrook, Chemical kinetics of hydrocarbon ignition in practical combustion systems, Proc. Combust. Inst. 28 (2000) 1563-1577.

[7] J.F. Griffiths, K.J. Hughes, R. Porter, The role and rate of hydrogen peroxide decomposition during hydrocarbon two-stage autoignition, Proc. Combust. Inst. 30 (2005) 1083-1091.

[8] S. Tanaka, F. Ayala, J.C. Keck, A reduced chemical kinetic model for HCCI combustion of primary reference fuels in a rapid compression machine, Combust. Flame 133 (2003) 467-481.

[9] F. Slemr, G.W. Harris, D.R. Hastie, G.I. Mackay, H.I. Schiff, Measurement of gas phase hydrogen peroxide in air by tunable diode laser absorption spectroscopy, J. Geophys. Res.-Atmos. 91 (1986) 5371-5378.

[10] J.D. DeSain, A.D. Ho, C.A. Taatjes, High-resolution diode laser absorption spectroscopy of the O–H stretch overtone band $(2,0,0) \leftarrow (0,0,0)$ of the HO_2 radical, J. Mol. Spectrosc. 219 (2003) 163-169.

[11] J. Thiébaud, C. Fittschen, Near infrared cw-CRDS coupled to laser photolysis: Spectroscopy and kinetics of the HO_2 radical, Appl. Phys. B 85 (2006) 383-389.

[12] N. Ibrahim, J. Thiebaud, J. Orphal, C. Fittschen, Air-broadening coefficients of the HO_2 radical in the $2\nu_1$ band measured using cw-CRDS, J. Mol. Spectrosc. 242 (2007) 64-69.

[13] J. Thiebaud, S. Crunaire, C. Fittschen, Measurements of line strengths in the $2\nu_1$ band of the HO_2 radical using laser photolysis/continuous wave cavity ring-down spectroscopy (cw-CRDS), J. Phys. Chem. A 111 (2007) 6959-6966.

[14] E.C. Tuazon, Atmospheric Measurements of Trace Pollutants by Kilometer-pathlength FT-IR Spectroscopy, Wiley1980.

[15] P.L. Hanst, N.W. Wong, J. Bragin, A long-path infra-red study of Los Angeles smog, Atmos. Environ. 16 (1982) 969-981.

[16] C. L. Hagen, S. T. Sanders, Investigation of multi-species (H_2O_2 and H_2O) sensing and thermometry in an HCCI engine by wavelength-agile absorption spectroscopy, Meas. Sci. Technol. 18 (2007) 1992.

[17] M.B. Sajid, E. Es-sebbar, T. Javed, C. Fittschen, A. Farooq, Measurement of the rate of hydrogen peroxide thermal decomposition in a shock tube using quantum cascade laser absorption near 7.7 μm, Int. J. Chem. Kinet. 46 (2014) 275-284.

[18] K. Kohse-Höinghaus, Laser techniques for the quantitative detection of reactive intermediates in combustion systems, Progr. Energy Combust. Sci. 20 (1994) 203-279.

[19] M. Aldén, J. Bood, Z. Li, M. Richter, Visualization and understanding of combustion processes using spatially and temporally resolved laser diagnostic techniques, Proc. Combust. Inst. 33 (2011) 69-97.

[20] Z.T. Cai, D.H. Zhang, J.Z.H. Zhang, Quantum dynamical studies for photodissociation of H2O2 at 248 and 266 nm, J. Chem. Phys. 100 (1994) 5631-5638.

[21] H. Okabe, Photochemistry of Small Molecules, John Wiley and Sons, New York, 1978.

[22] M.O. Rodgers, K. Asai, D.D. Davis, Photofragmentation-laser induced fluorescence: a new method for detecting atmospheric trace gases, Appl. Opt. 19 (1980) 3597-3605.

[23] J.B. Simeonsson, R.C. Sausa, A critical review of laser photofragmentation/fragment detection techniques for gas-phase chemical analysis, Appl. Spectrosc. Rev. 31 (1996) 1-72.

[24] J.B. Simeonsson, R.C. Sausa, Laser photofragmentation/fragment detection techniques for chemical analysis of the gas phase, Trends Analyt. Chem. 17 (1998) 542-550.

[25] B. Li, M. Jonsson, M. Algotsson, J. Bood, Z.S. Li, O. Johansson, M. Aldén, M. Tunér, B. Johansson, Quantitative detection of hydrogen peroxide in an HCCI engine using photofragmentation laser-induced fluorescence, Proc. Combust. Inst. 34 (2013) 3573-3581.

[26] G. Coskun, M. Jonsson, J. Bood, M. Tunér, M. Algotsson, B. Li, Z. Li, H.S. Soyhan, M. Aldén, B. Johansson, Analysis of in-cylinder H_2O_2 and HO_2 distributions in an HCCI engine – Comparison of laser-diagnostic results with CFD and SRM simulations, Combust. Flame 162 (2015) 3131-3139.

[27] O. Johansson, J. Bood, B. Li, A. Ehn, Z.S. Li, Z.W. Sun, M. Jonsson, A.A. Konnov, M. Aldén, Photofragmentation laser-induced fluorescence imaging in premixed flames, Combust. Flame 158 (2011) 1908-1919.

[28] K. Larsson, M. Jonsson, J. Borggren, E. Kristensson, A. Ehn, M. Aldén, J. Bood, Single-shot photofragment imaging by structured illumination, Opt. Lett 40 (2015) 5019-5022.

[29] A. Sinha, J. Coleman, R. Barnes, Photodissociation dynamics of HO_2 at 220 nm: Determination of the O(^{1}D):O(^{3}P) branching ratio, J. Phys. Chem. 98 (1994) 12462-12465.

[30] L.C. Lee, H. Helm, J.S. Chang, $O_2(b^1\Sigma_g^+ \rightarrow X^3\Sigma_g^-)$ emission following HO_2 photodissociation by KrF laser photons, Chem. Phys. Lett. 81 (1981) 537-540.

[31] L.C. Lee, Observation of O(^{1}D) produced from photodissociation of HO_2 at 193 and 248 nm, J. Chem. Phys. 76 (1982) 4909-4915.

[32] A.A. Konnov, Implementation of the NCN pathway of prompt-NO formation in the detailed reaction mechanism, Combust. Flame 156 (2009) 2093-2105.

[33] K. Takahashi, Y. Takeuchi, Y. Matsumi, Rate constants of the O(^{1}D) reactions with N_2, O_2, N_2O, and H_2O at 295 K, Chem. Phys. Lett. 410 (2005) 196-200.

[34] A. Lifshitz, J.V. Michael, Rate constants for the reaction, O+$H_2O\rightarrow$OH+OH, over the temperature range, 1500–2400 K, by the flash photolysis-shock tube technique: A further consideration of the back reaction, Symp. (Int.) Combust. 23 (1991) 59-67.

[35] S. Vranckx, J. Peeters, S. Carl, A temperature dependence kinetic study of O(^{1}D)+ CH_4: overall rate coefficient and product yields, Phys. Chem. Chem. Phys. 10 (2008) 5714-5722.

[36] D.L. Baulch, C.J. Cobos, R.A. Cox, C. Esser, P. Frank, T. Just, J.A. Kerr, M.J. Pilling, J. Troe, R.W. Walker, J. Warnatz, Evaluated kinetic data for combustion modelling, J. Phys. Chem. Ref. Data 21 (1992) 411-734.

[37] M.A. Blitz, T.J. Dillon, D.E. Heard, M.J. Pilling, I.D. Trought, Laser induced fluorescence studies of the reactions of O(^{1}D_2) with N_2, O_2, N_2O, CH_4, H_2, CO_2, Ar, Kr and n-C_4H_{10}, Phys. Chem. Chem. Phys. 6 (2004) 2162-2171.

[38] N.K. Srinivasan, M.C. Su, J.W. Sutherland, J.V. Michael, Reflected shock tube studies of high-temperature rate constants for OH + $CH_4 \rightarrow CH_3 + H_2O$ and $CH_3 + NO_2 \rightarrow CH_3O + NO$, J. Phys. Chem. A 109 (2005) 1857-1863.

[39] M. Kotzagianni, S. Couris, Femtosecond laser induced breakdown for combustion diagnostics, Appl. Phys. Lett. 100 (2012) 264104.

[40] F. Kong, Q. Luo, H. Xu, M. Sharifi, D. Song, S.L. Chin, Explosive photodissociation of methane induced by ultrafast intense laser, J. Chem. Phys. 125 (2006) 133320.

[41] M. Jonsson, J. Borggren, M. Aldén, J. Bood, Time-resolved spectroscopic study of photofragment fluorescence in methane/air mixtures and its diagnostic implications, Appl. Phys. B 120 (2015) 587-599.

[42] J. Luque, D.R. Crosley, LIFBASE: Database and spectral simulation (version 1.5), SRI International Report MP 99-009, 1999.

[43] J.B. Jeffries, C. Schulz, D.W. Mattison, M.A. Oehlschlaeger, W.G. Bessler, T. Lee, D.F. Davidson, R.K. Hanson, UV absorption of CO2 for temperature diagnostics of hydrocarbon combustion applications, Proc. Combust. Inst. 30 (2005) 1591-1599.

[44] B. Ruscic, R.E. Pinzon, M.L. Morton, N.K. Srinivasan, M.-C. Su, J.W. Sutherland, J.V. Michael, Active thermochemical tables: Accurate enthalpy of formation of hydroperoxyl radical, HO_2, .J. Phys. Chem. A 110 (2006) 6592-6601.

[45] D.L. Baulch, R.A. Cox, P.J. Crutzen, R.F. Hampson, J.A. Kerr, J. Troe, R.T. Watson, Evaluated kinetic and photochemical data for atmospheric chemistry: Supplement I, J. Phys. Chem. Ref. Data 11 (1982) 327-496.

[46] V. Sick, N. Wermuth, Single-shot imaging of OH radicals and simultaneous OH radical/acetone imaging with a tunable Nd : YAG laser, Appl. Phys. B 79 (2004) 139-143.

[47] R. Atkinson, D. Baulch, R. Cox, J. Crowley, R. Hampson, R. Hynes, M. Jenkin, M. Rossi, J. Troe, Evaluated kinetic and photochemical data for atmospheric chemistry: Volume I - gas phase reactions of O_x, HO_x, NO_x and SO_x species, Atmos. Chem. Phys. 4 (2004) 1461-1738.

[48] A. Rodriguez, O. Frottier, O. Herbinet, R. Fournet, R. Bounaceur, C. Fittschen, F. Battin-Leclerc, Experimental and modeling investigation of the low-temperature oxidation of dimethyl ether, J. Phys. Chem. A 119 (2015) 7905-7923.